

Galactic Winds with MUSE: A Direct Detection of Fe II* Emission from a $z = 1.29$ Galaxy [★]

Hayley Finley^{1,2}, Nicolas Bouché³, Thierry Contini^{1,2}, Benoît Epinat^{1,2,4}, Roland Bacon⁵, Jarle Brinchmann^{6,7}, Sebastiano Cantalupo⁸, Santiago Erroz-Ferrer⁸, Raffaella Anna Marino⁸, Michael Maseda⁶, Johan Richard⁵, Anne Verhamme^{5,9}, Peter M. Weilbacher¹⁰, Martin Wendt^{10,11}, and Lutz Wisotzki¹⁰

¹ Université de Toulouse, UPS-OMP, 31400 Toulouse, France e-mail: hayley.finley@irap.omp.eu

² IRAP, Institut de Recherche en Astrophysique et Planétologie, CNRS, 14 avenue Édouard Belin, 31400 Toulouse, France

³ IRAP, Institut de Recherche en Astrophysique et Planétologie, CNRS, 9 avenue Colonel Roche, 31400 Toulouse, France

⁴ Aix Marseille Univ, CNRS, LAM, Laboratoire d'Astrophysique de Marseille, Marseille, France

⁵ CRAL, Observatoire de Lyon, CNRS, Université Lyon 1, 9 Avenue Ch. André, F-69561 Saint Genis Laval Cedex, France

⁶ Leiden Observatory, Leiden University, P.O. Box 9513, 2300 RA Leiden, The Netherlands

⁷ Instituto de Astrofísica e Ciências do Espaço, Universidade do Porto, CAUP, Rua das Estrelas, PT4150-762 Porto, Portugal

⁸ ETH Zurich, Institute of Astronomy, Wolfgang-Pauli-Str. 27, CH-8093 Zürich, Switzerland

⁹ Observatoire de Genève, Université de Genève, 51 Ch. des Maillettes, 1290 Versoix, Switzerland

¹⁰ Leibniz-Institut für Astrophysik Potsdam (AIP), An der Sternwarte 16, D-14482 Potsdam, Germany

¹¹ Institut für Physik und Astronomie, Universität Potsdam, Karl-Liebknecht-Str. 24/25, 14476 Golm, Germany

ABSTRACT

Emission signatures from galactic winds provide an opportunity to directly map the outflowing gas, but this is traditionally challenging because of the low surface brightness. Using very deep observations (27 hours) of the *Hubble* Deep Field South with the Multi Unit Spectroscopic Explorer (MUSE) instrument, we identify signatures of an outflow in both emission and absorption from a spatially resolved galaxy at $z = 1.29$ with a stellar mass $M_{\star} = 8 \times 10^9 M_{\odot}$, star formation rate $\text{SFR} = 77^{+40}_{-25} M_{\odot} \text{ yr}^{-1}$, and star formation rate surface brightness $\Sigma_{\text{SFR}} = 1.6 M_{\odot} \text{ kpc}^{-2}$ within the [O II] $\lambda\lambda 3727, 3729$ half-light radius $R_{1/2, [\text{O II}]} = 2.76 \pm 0.17 \text{ kpc}$. From a component of the strong resonant Mg II and Fe II absorptions at -350 km s^{-1} , we infer a mass outflow rate that is comparable to the star formation rate. We detect non-resonant Fe II* emission, at $\lambda 2626, \lambda 2612, \lambda 2396, \text{ and } \lambda 2365$, at $1.2 - 2.4 - 1.5 - 2.7 \times 10^{-18} \text{ egs s}^{-1} \text{ cm}^{-2}$ respectively. These flux ratios are consistent with the expectations for optically thick gas. By combining the four non-resonant Fe II* emission lines, we spatially map the Fe II* emission from an individual galaxy for the first time. The Fe II* emission has an elliptical morphology that is roughly aligned with the galaxy minor kinematic axis, and its integrated half-light radius, $R_{1/2, \text{Fe II}^*} = 4.1 \pm 0.4 \text{ kpc}$, is 50% larger than the stellar continuum ($R_{1/2, \star} \approx 2.34 \pm 0.17$) or the [O II] nebular line. Moreover, the Fe II* emission shows a blue wing extending up to -400 km s^{-1} , which is more pronounced along the galaxy minor kinematic axis and reveals a C-shaped pattern in a $p - v$ diagram along that axis. These features are consistent with a bi-conical outflow.

Key words. Galaxies: evolution – Galaxies: starburst – Galaxies: ISM – ISM: jets and outflows – Ultraviolet: ISM

1. Introduction

Galactic winds, driven by the collective effect of hot stars and supernovae explosions, play a major role in regulating galaxy evolution. By expelling enriched matter beyond the halo, galactic winds can address discrepancies between observations and ΛCDM models that over-predict the number of low-mass galaxies (Silk & Mamon 2012) and enrich the intergalactic medium (Oppenheimer & Davé 2008; Ford et al. 2016). Likewise, galactic winds may play a major role in regulating the mass-metallicity relation (Finlator & Davé 2008; Lilly et al. 2013; Tremonti et al. 2004). Therefore, quantifying the mass fluxes of galactic outflows (and their extents) is necessary to gain a complete understanding of galaxy evolution.

However, while galactic winds appear ubiquitous (e.g., Veilleux et al. 2005; Weiner et al. 2009; Steidel et al. 2010; Ru-

bin et al. 2010b, 2014; Martin et al. 2012; Heckman et al. 2015; Zhu et al. 2015; Chisholm et al. 2015), observational constraints for the physical properties of galactic outflows, including their extents and mass outflow rates, are sparse. Traditional "down the barrel" 1D galaxy spectroscopy provides direct constraints on the wind speed from the blue-shifted absorption lines but cannot constrain the physical extent of outflows, leading to large uncertainties in outflow rates. Techniques that use a background source can address this question.

For instance, the background quasar technique provides constraints on the physical extent of gas flows from the impact parameter between the galaxy and the absorbing gas (e.g. Bouché et al. 2012; Kacprzak et al. 2012; Schroetter et al. 2015, 2016; Péroux et al. 2016; Bouché et al. 2016; Straka et al. 2016). These recent studies have made progress investigating the kinematics, orientation, and extent of gas flows around star forming galaxies. As a variation on this technique, spectroscopy against a background galaxy probes absorption from the foreground galaxy halo over a larger solid angle (e.g., Adelberger et al. 2005; Rubin et al. 2010a; Steidel et al. 2010; Bordoloi et al. 2011, 2014;

[★] Based on observations of the *Hubble* Deep Field South made with ESO telescopes at the La Silla Paranal Observatory under program ID 60.A-9100(C). Advanced data products are available at <http://muse.vlt.eu/science>.

Diamond-Stanic et al. 2016). However, these constraints on the physical extent of outflows are usually limited due to their one-dimensional nature, except for Cazzoli et al. (2016). Mapping the extent of gas flows in two dimensions is critical to better constrain mass outflow rates.

Mapping outflows in emission, such as for M82 (e.g., Shopbell & Bland-Hawthorn 1998; Lehnert et al. 1999) and other nearby galaxies (e.g., Heckman et al. 1995; Cecil et al. 2001; Veilleux & Rupke 2002; Matsubayashi et al. 2009; Moiseev et al. 2010), is difficult at high redshift, because the emitting gas inherently has a very low surface brightness. Beyond the local universe, galaxies with emission signatures from outflows are beginning to be detected. Currently, rest-frame UV and optical spectroscopy use three types of emission signatures to map the extent of outflows: the nebular, resonant, and non-resonant emission lines. The most common nebular emission lines seen in H II regions are hydrogen recombination and forbidden lines, such as [O II] $\lambda\lambda 3727, 3729$. A transition is resonant when a photon can be absorbed from the ground state and re-emitted to the same lowest level of the ground state, as for Lyman-alpha and the Mg II $\lambda\lambda 2796, 2803$ transitions. A transition is non-resonant when the photon can be re-emitted to an excited level of a ground state that has multiple levels due to fine structure splitting. Non-resonant transitions are commonly denoted with a *, like Fe II*. Due to the slight energy difference between the ground and excited states, photons from non-resonant emission no longer have the correct wavelength to be re-absorbed through a resonant transition and instead escape. In other words, the gas is optically thin to photons that are emitted through a non-resonant transition.

The first type of emission signature (nebular lines) from outflows can appear as a broad component in nebular emission lines such as H α . Such broad component is regularly seen in local Ultra-Luminous Infra-Red Galaxies (ULIRGs, e.g. Soto & Martin 2012; Arribas et al. 2014; García-Burillo et al. 2015) and more recently in normal star-forming galaxies (Wood et al. 2015; Cicone et al. 2016). At high redshifts, Newman et al. (2012) detected a broad H α component in composite spectra of $z \sim 2$ star-forming galaxies and Genzel et al. (2011) observed this broad component in a few individual galaxies. Newman et al. (2012) found that the broad emission is spatially extended beyond the half-light radius, $R_{1/2}$.

The second possible emission signature of outflows comes from resonant transitions such as Ly α , a line which is often more extended than the stellar continuum (e.g. Steidel et al. 2011; Matsuda et al. 2012; Wisotzki et al. 2016) but might be strongly affected by dust absorption. Emission from resonant metal lines, such as Si II, Fe II, or Mg II, is less affected by dust and may be observed as P-cygni profiles. The relative strength between the (mostly) blueshifted absorption and (mostly) redshifted emission dictates whether the signature appears as a traditional P-cygni profile or as emission ‘infilling’. Contrary to the resonant Fe II lines observed across a similar wavelength range (Fe II $\lambda\lambda 2344, \lambda\lambda 2374, 2382$, and $\lambda\lambda 2586, 2600$), the Mg II doublet is particularly sensitive to emission infilling, since its lower energy level does not have fine structure splitting. As a result of the different possible relative strengths of the emission and absorption components, observed profiles for the resonant Mg II $\lambda\lambda 2796, 2803$ transitions vary greatly for different star-forming galaxies (Weiner et al. 2009; Rubin et al. 2011; Coil et al. 2011; Erb et al. 2012; Martin et al. 2012, 2013; Kornei et al. 2013).

The third possible signature of outflows in emission is from non-resonant transitions such as C II*, Si II* (e.g., Shapley et al. 2003) or Fe II* (e.g., Rubin et al. 2011). Detecting non-resonant

emission typically requires stacking hundreds of galaxy spectra. Using more than 800 Lyman break galaxies (LBGs) at $z > 2$, Shapley et al. (2003) first detected Si II* in the composite spectrum, and Berry et al. (2012) more recently detected C II* and Si II* in the composite spectrum of 59 LBGs. Since the non-resonant Fe II* lines are at redder wavelengths than C II* and Si II*, they are practical for investigating outflows at lower redshifts, like $z \sim 1$. Based on comparing composite spectra from samples of ~ 100 or more star-forming galaxies at $z \sim 1 - 2$ (Erb et al. 2012; Kornei et al. 2013; Tang et al. 2014), Fe II* emission may vary with galaxy properties, such as galaxy mass and dust attenuation. Coil et al. (2011) present individual spectra with different combinations of blue-shifted absorption, resonant Mg II emission, and non-resonant Fe II*. In two notable direct detections of Fe II* emission from galaxies at $z = 0.694$ and $z = 0.9392$ (Rubin et al. 2011; Martin et al. 2012), the non-resonant emission is observed along with blue-shifted absorption lines and resonant Mg II emission, allowing the authors to constrain and model the outflows. Similarly, Jaskot & Oey (2014) use non-resonant C II* and Si II* emission in UV spectra of four green pea galaxies at $z \sim 0.14 - 0.2$ to infer the geometry of their outflows.

These studies provide information about outflow properties on galactic scales, but it is also possible to characterize outflows from individual star-forming regions across $z > 1$ galaxies thanks to adaptive optics or gravitational lensing (i.e., Genzel et al. 2011; Rigby et al. 2014; Karman et al. 2016; Bordoloi et al. 2016, Patricio et al. in prep.). Using adaptive optics, Genzel et al. (2011) identify star-forming regions in five $z > 2$ galaxies and argue that bright regions (or clumps) with a broad component in the nebular emission are the launch sites for massive galactic winds. With the benefit of gravitational lensing, Karman et al. (2016) characterize Mg II emission, Fe II* $\lambda\lambda 2612, 2626$ emission, and Fe II absorption from multiple star-forming regions across a supernova host galaxy at $z = 1.49$ at locations both associated with and independent of the supernovae explosion. Bordoloi et al. (2016) likewise detect blueshifted Fe II and Mg II absorptions, redshifted Mg II emission, and non-resonant Fe II* $\lambda\lambda 2612, 2626$ emission in four star-forming regions of a gravitationally lensed galaxy at $z = 1.70$, but find that the outflow properties vary from region to region. Spatially resolved observations suggest that outflow properties could be localized and strongly influenced by the nearest star-forming clump.

Despite advances from these diverse studies, we have not yet been able to map the morphology and extent of outflows from individual galaxies beyond the local universe. The new generation of integral field spectrographs, the Multi Unit Spectroscopic Explorer (MUSE; Bacon et al. 2015) on the VLT and the Keck Cosmic Web Imager (Morrissey et al. 2012), are well-suited for studying galactic winds in emission and tackling this challenge. While slit spectroscopy can inadvertently miss scattered emission if the aperture does not cover the full extent of the outflowing envelope (Scarlatà & Panagia 2015), integral field observations eliminate aperture effects for distant galaxies, making emission signatures easier to detect. The combined spatial and spectroscopic data facilitate characterizing the morphology and kinematics of both star-forming galaxies and the outflows they produce.

In this paper, we analyze galactic wind signatures from a spatially resolved star-forming galaxy at $z = 1.2902$ observed with MUSE. We present the observations in Section 2 and summarize the galaxy properties in Section 3. With the integrated 1D MUSE galaxy spectrum, we characterize outflow signatures from Fe II, Mg II, and Mg I transitions in absorption and Fe II* transitions in

emission in Section 4. We then investigate the spatial extent and the kinematic properties of the Fe II* emission in Sections 5 and 6, respectively. In Section 7, we compare our observations with radiative transfer wind models and estimate the mass outflow rate. We review our findings in Section 8. Throughout the paper, we assume a Λ CDM cosmology with $\Omega_m = 0.3$, $\Omega_\Lambda = 0.7$, and $H_0 = 70 \text{ km s}^{-1} \text{ Mpc}^{-1}$. With this cosmology, 1 arcsec corresponds to 8.37 kpc at the redshift of the galaxy.

2. Data

MUSE fully covers the wavelength range 4650 – 9300 Å with 1.25 Å per spectral pixel. The field of view spans $1' \times 1'$ with a pixel size of $0.2''$. The instrument is notable both for its high throughput, which reaches 35% at 7000 Å (end-to-end including the telescope), and its excellent image quality sampled at $0.2''$ per spaxel. While MUSE opens new avenues to address a wide variety of scientific questions, these two characteristics make the instrument optimal for deep field observations.

As part of commissioning data taken during July and August 2014, MUSE observed a $1' \times 1'$ field of view in the Hubble Deep Field South (HDFS) for a total integration time of 27 hours. The final data cube is a 5σ -clipped mean of 54 individual exposures that were taken in dark time under good seeing conditions ($0.5'' - 0.9''$). The 1σ emission-line surface brightness limit for this cube is $1 \times 10^{-19} \text{ erg s}^{-1} \text{ cm}^{-2} \text{ arcsec}^{-2}$. The MUSE observations provided spectroscopic redshifts for 189 sources with magnitude $I_{814} \leq 29.5$ (8 stars and 181 galaxies), a factor-of-ten increase over the 18 previously-measured spectroscopic redshifts in this field. A catalogue of sources in the MUSE HDFS field includes the redshifts, emission-line fluxes, and 1D spectra. The observations, the data cube, and an overview of scientific exploitations are fully described in Bacon et al. (2015). Both the data cube and the catalogue of sources are publicly available.¹

The deep IFU observations reveal emission from Fe II* transitions directly detected from one galaxy in the MUSE HDFS. The galaxy has ID #13 in the MUSE catalogue, with coordinates $\alpha = 22\text{h } 32\text{m } 52.16\text{s}$, $\delta = -60^\circ 33' 23.92''$ (J2000) and magnitude $I_{814} = 22.83 \pm 0.005$. It is part of a 9-member group at $z \approx 1.284$, discussed in Bacon et al. (2015), that also includes two AGN and an interacting system with tidal tails. This direct detection of a galaxy with Fe II* emission offers a new opportunity to characterize galactic winds.

3. Galaxy Properties

Galaxy ID#13 is part of a sample of 28 spatially resolved galaxies that Contini et al. (2016) selected from the MUSE HDFS according to the criterion that the brightest emission line covers at least 20 spatial pixels with a signal-to-noise ratio (S/N) higher than 15. For this galaxy, emission from the [O II] $\lambda\lambda 3727, 3729$ doublet is the dominant feature in the MUSE spectrum. We determined the galaxy systemic redshift from a p - v diagram extracted from the MUSE data cube along the galaxy kinematic major axis by fitting a double Gaussian profile to the [O II] $\lambda\lambda 3727, 3729$ emission at each position along the slit. The systemic redshift of $z = 1.29018 \pm 0.00006$ is the mean value between the two asymptotes of the rotation curve.

Contini et al. (2016) investigated the morphological and kinematic properties of the galaxy ID#13, as part of the MUSE HDFS spatially resolved galaxy sample. They constrained the

Table 1. Galaxy ID#13 properties from Contini et al. (2016)

Morphological Analysis	HST + GALFIT
Position angle ($^\circ$)	-45.9 ± 1.9
Inclination i ($^\circ$)	33 ± 5
Half-light radius (kpc)	2.1 ± 0.03
Kinematic Analysis	MUSE 2D/3D
Position angle ($^\circ$)	$-14/-13$
Inclination i ($^\circ$)	$+28/+17$
Max. rotational velocity (km s^{-1})	$+24/+44$
Velocity dispersion (km s^{-1})	$+48/+46$
Photometric Analysis	SED fitting
Visual extinction A_V (mag)	$1.20^{+0.59}_{-0.26}$
$\log(M_\star)$ (M_\odot)	9.89 ± 0.11
$\log(\text{SFR})$ ($M_\odot \text{ yr}^{-1}$)	1.89 ± 0.18

morphology from HST images in the F814W band by modelling the galaxy with GALFIT (Peng et al. 2002) as a bulge plus an exponential disk. Contini et al. (2016) then performed the kinematic analysis with two different techniques: a traditional 2D line-fitting method with the Camel algorithm (Epinat et al. 2012; Contini et al. 2016) combined with a 2D rotating disk model, which requires prior knowledge of the galaxy inclination, and a 3D fitting algorithm, GalPaK^{3D} (Bouché et al. 2015), which simultaneously fits the morphological and kinematic parameters directly from the MUSE data cube. The parameters from the 2D and 3D models are in good agreement overall (see Table 1).

From the morphological analysis on the HST images, galaxy ID#13 is compact with a disk scale length of $R_d = 1.25 \text{ kpc}$ (correspondingly $R_{1/2} = 2.1 \text{ kpc}$) and has a low inclination angle of $i = 33^\circ$. The inclination from 3D fitting yields a lower value of $\sim 20^\circ$. The disagreement likely arises from an asymmetric morphology seen in the HST images, since statistically the two techniques measure inclinations that are in good agreement (Contini et al. 2016). The galaxy also shows a misalignment between the morphological position angle measured from the HST image, -46° , and the MUSE kinematic position angle, -13° , again likely due to the asymmetric light distribution that only appears at higher spatial resolution. Regardless, the galaxy has a low inclination with $i \sim 20^\circ - 30^\circ$.

From the kinematic analysis on the MUSE data, the velocity field has a low gradient, $\pm 10 \text{ km s}^{-1}$, a low maximum velocity, 24 km s^{-1} , and a velocity dispersion of $45 - 50 \text{ km s}^{-1}$. Therefore, non-circular motions dominate the gas dynamics within the disk, with $V/\sigma \approx 0.5$, i.e. below the commonly-used $V/\sigma \leq 1$ threshold for identifying dispersion-dominated galaxies. Note that the different maximum velocities from the 2D and 3D methods are entirely due to the different inclination values (Table 1). Nonetheless, the ratio remains $V/\sigma \lesssim 1$ for the range of possible inclinations, $17^\circ - 33^\circ$.

Contini et al. (2016) estimated the visual extinction, $A_V = 1.20 \text{ mag}$, stellar mass, $M_\star = 8 \times 10^9 M_\odot$, and star formation rate $\text{SFR} = 77^{+40}_{-25} M_\odot \text{ yr}^{-1}$, from Stellar Population Synthesis using broad-band visible and near infra-red photometry². The galaxy ID#13 is one of the most massive of the 28 spatially-resolved galaxies in the MUSE HDFS sample and also has the highest star formation rate (SFR). This SFR places galaxy ID#13 above the main sequence (Elbaz et al. 2007; Karim et al. 2011; Whitaker et al. 2014; Tomczak et al. 2016) by almost 1 dex, indicating that

² The [OII]-derived SFR for a Chabrier (2003) IMF is $65 M_\odot \text{ yr}^{-1}$ using the Kewley et al. (2004) calibration, which also yields an extinction of $A_V = 1.5$ in the gas.

¹ <http://muse-vlt.eu/science/hdfs-v1-0/>

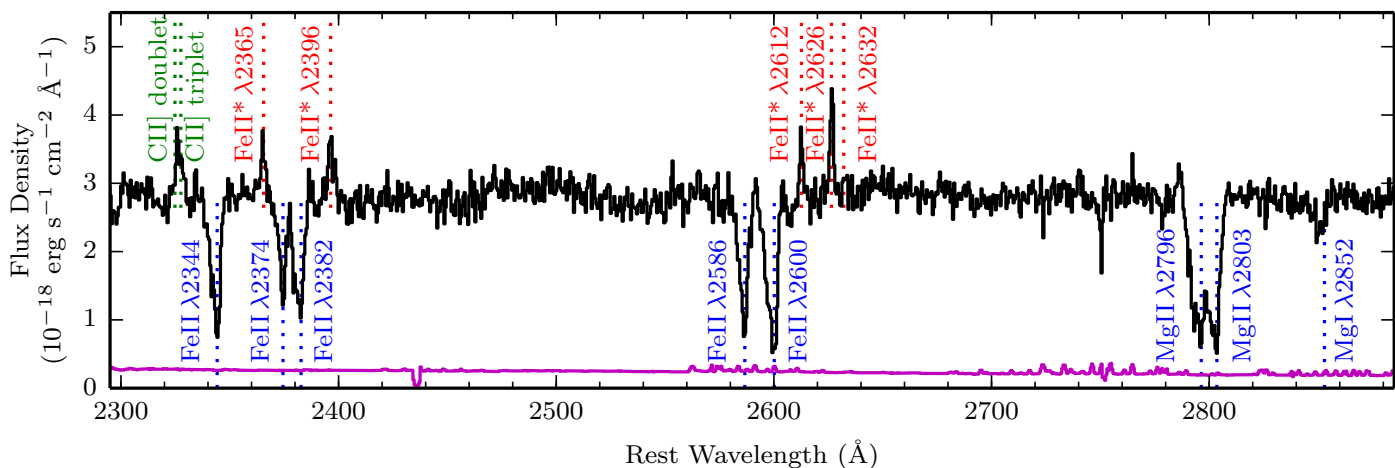


Fig. 1. Vacuum rest-frame 1D spectrum of the MUSE HDFs galaxy ID#13 covering the Fe II and Mg II transitions. The spectrum is in black with the 1σ error in magenta. Resonant transitions detected in absorption are labeled in blue. Non-resonant Fe II* transitions detected in emission are labeled in red. The C II] nebular emission, which is a blend of five transitions, is labeled in green.

this galaxy is undergoing a starburst with a high specific SFR of $sSFR = 10 \text{ Gyr}^{-1}$. The starburst phase of galaxy evolution can produce large-scale outflows when many short-lived massive stars explode as supernovae.

The properties of this galaxy are conducive to detecting signatures from galactic winds. The low inclination angle favors observing blue-shifted absorptions, given that this signature increases substantially towards face-on galaxies (Chen et al. 2010; Kornei et al. 2012; Rubin et al. 2014). The [O II] luminosity ($\sim 10^{43} \text{ erg s}^{-1}$) and rest-frame equivalent width ($\sim 50 \text{ \AA}$, see Table 3) indicate that the galaxy ID#13 is also well-suited for investigating winds in emission, since Fe II* and Mg II emission correlate with $L_{\text{O II}}$ or [O II] rest-frame equivalent width (Kornei et al. 2013; Zhu et al. 2015).

4. Absorption and emission profiles from the 1D spectrum

In this section, we analyze the galaxy ID#13 1D spectrum extracted from the MUSE data using a white-light weighting scheme. The 1D MUSE spectrum (Figure 1) reveals resonant Fe II, Mg II, and Mg I self-absorption, non-resonant Fe II* emission, and C II] and [O II] nebular emission lines. The Fe II transitions occur in three multiplets³. In the Fe II UV1, UV2, and UV3 multiplets, a photon can be re-emitted either through a resonant transition to the ground state, which produces emission infilling, or through a non-resonant transition to an excited state in the lower level, in which case the emission occurs at a slightly different wavelength. We investigate the integrated absorption and emission profiles, focusing first on the resonant absorption and emission properties (Section 4.1), then on the non-resonant emission properties (Section 4.2).

4.1. Resonant Fe and Mg profiles

Figure 2 compares the velocity profiles of each of the individual Fe II, Mg II, and Mg I transitions relative to the galaxy systemic redshift. The self-absorption profiles are asymmetric, with the strongest component centered on the galaxy systemic redshift, and a significant blue wing extending to -800 km s^{-1} .

We fit these profiles simultaneously with VPFIT⁴ v10, using several components and requiring each to have the same redshift and Doppler parameter across the different transitions. The absorptions are well-fitted with three components at redshifts 1.28514 ± 0.00021 , 1.28752 ± 0.00009 , and 1.29024 ± 0.00006 , corresponding to shifts of $-660 \pm 28 \text{ km s}^{-1}$, $-349 \pm 12 \text{ km s}^{-1}$ and $+8.5 \pm 6.5 \text{ km s}^{-1}$ relative to the galaxy systemic velocity. Table 2 summarizes the total rest-frame equivalent widths for each transition, calculated both from the fit and directly from the flux.

Globally, the Fe II resonant transitions in Figure 2 reveal several key features: (1) the Fe II profiles are very similar to one another, and (2) the strongest component is roughly centered at the galaxy systemic redshift. As Prochaska et al. (2011) first demonstrated, emission infilling in resonant absorption lines can alter doublet ratios and mimic partial coverage. However, here we find that emission infilling does not play a significant role in this galaxy for the following two qualitative arguments.

First, while strong emission infilling would produce clear P-cygni profiles (which are not observed), moderate amounts of emission infilling would cause a blue-shift to the centroid of the absorption, an effect commonly seen in stacked spectra (e.g., Zhu et al. 2015) or individual cases (Rubin et al. 2011; Martin et al. 2013). None of the absorptions in the galaxy ID#13 spectrum (Figure 2) have blue-shifted centroids.

Second, because Fe II has multiple channels to re-emit the photons (through resonant and non-resonant transitions), the degree of infilling for a particular Fe II absorption line depends on the likelihood of re-emission through the different channels within a multiplet. Purely resonant transitions, such as Mg II and Fe II $\lambda 2383$, are the most sensitive to emission infilling. Zhu et al. (2015) demonstrated that the Fe II resonant absorptions that are the least (most) affected by emission infilling are Fe II $\lambda 2374$ (Fe II $\lambda 2600$ and Fe II $\lambda 2383$) respectively. Figure 2 shows that the Fe II $\lambda 2374$, $\lambda 2600$ and $\lambda 2383$ absorption profiles are all very similar for the galaxy ID#13. The lack of blue-shifted centroids and the consistent absorption profiles argue strongly against the presence of detectable emission infilling in this galaxy.

We quantify (and put a limit on) the global amount of infilling using the method proposed by Zhu et al. (2015), which consists of comparing the observed rest-frame equivalent widths

³ See Tang et al. (2014) or Zhu et al. (2015) for energy level diagrams.

⁴ <http://www.ast.cam.ac.uk/~rfc/vpfit.html>

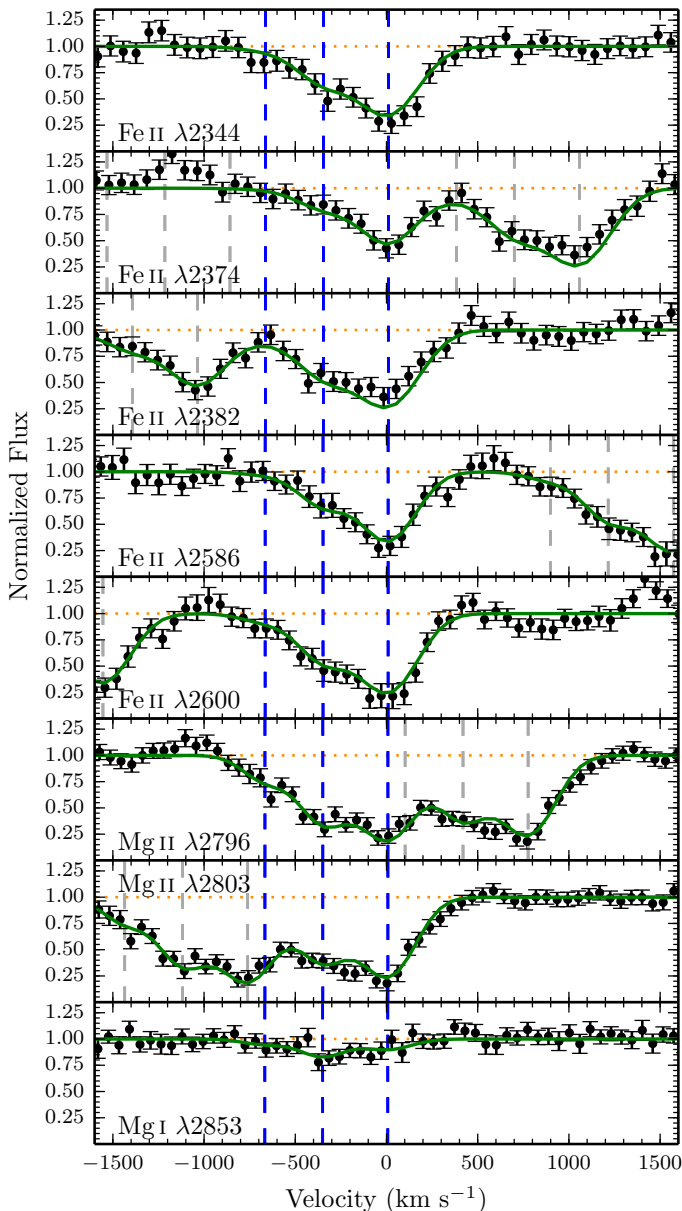


Fig. 2. Fe II, Mg II, and Mg I transitions detected in absorption in the 1D MUSE spectrum. Error bars show the $1\text{-}\sigma$ error on the flux (black), and the green curve traces the fit to the absorption profiles. Zero velocity is relative to the galaxy systemic redshift, $z = 1.2902$. Vertical blue dashed lines mark the three components used to fit each absorption, and gray dashed lines show components that are part of neighboring transitions. The asymmetric absorption profiles indicate significant blue-shifted absorption.

of the resonant lines to those seen in intervening quasar spectra (see their Figure 12). Using the averaged rest-frame equivalent widths of resonant Fe II and Mg II absorptions from a stacked spectrum of ~ 30 strong Mg II absorber galaxies at $0.5 < z < 1.5$ from Dutta et al. (2017, their Table 7), we find that our data is consistent with no emission infilling. Our data could allow for at most $< 0.8 \text{ \AA}$ ($< 1.8 \text{ \AA}$) of infilling for Fe II $\lambda 2600$ (Fe II $\lambda 2383$), the two transitions most susceptible to infilling (Zhu et al. 2015). This means that at most 22% (55%) of these absorptions could be affected by infilling and that the impact on the other Fe II absorptions is even smaller.

Similarly, we separately estimate the amount of infilling for each of the three sub-components shown in Figure 2 (Table 2).

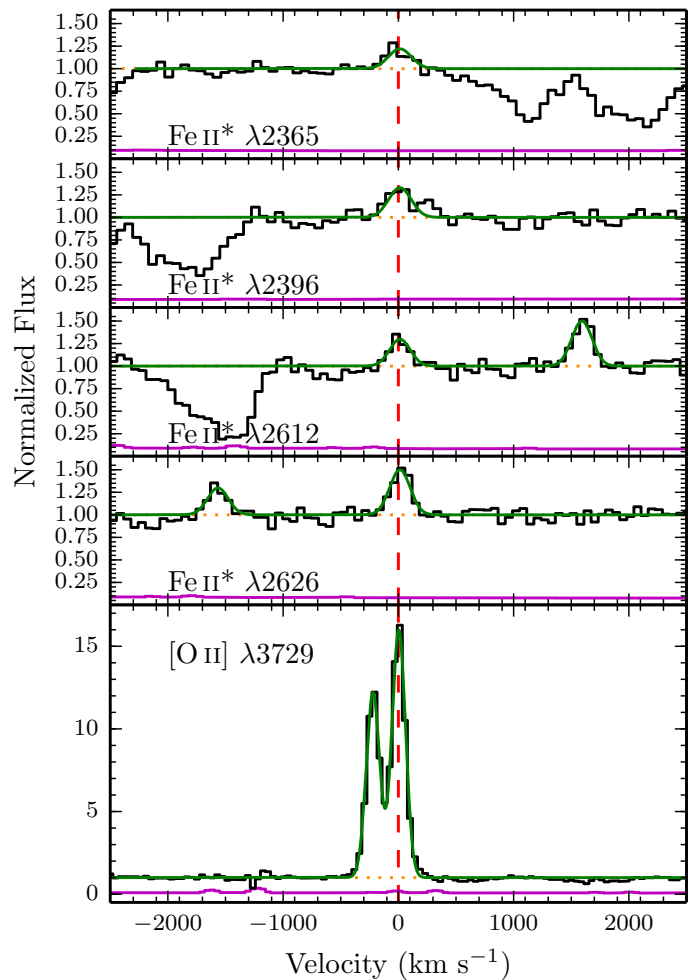


Fig. 3. Fe II* and [O II] emission peaks detected in the normalized 1D MUSE spectrum. The green curve traces joint Gaussian fits to the four Fe II* emission peaks and the [O II] doublet, respectively. Zero velocity, indicated with the vertical red dashed line, is relative to the galaxy systemic redshift, $z = 1.2902$, measured from the [O II] emission.

We are unable to put constraints on the weak component ‘A’, but the blue-shifted component ‘B’ at -350 km s^{-1} does not allow for emission infilling that would increase the Fe II $\lambda 2383$ equivalent width by more than 10%. The component ‘C’ at the galaxy systemic redshift allows for the largest amount of emission infilling with 60% corrections for Fe II $\lambda 2600$ and Fe II $\lambda 2383$, 40% for Fe II $\lambda 2344$ and 20% for Fe II $\lambda 2586$. As we discuss later in Section 7.2, the blue-shifted galactic wind component (‘B’) appears to be less affected by emission infilling than the systemic component associated with the galaxy ISM (‘C’).

We end this section by mentioning that, as we will argue in section 7.2, the Fe II and Mg II gas is likely optically thick. The absorptions ought to be saturated, and the reason we do not observe fully absorbed profiles is either due to a partial covering fraction (rather than emission infilling) or more likely to the low spectral resolution. As we will show in the next section, the non-resonant Fe II* emission pattern is also consistent with optically thick gas.

4.2. Non-resonant emission

Figure 3 shows the non-resonant transitions Fe II* $\lambda 2365$, $\lambda 2396$, $\lambda 2612$, and $\lambda 2626$ that we detect in the MUSE HDFS galaxy

ID#13 1D spectrum at $2.5\sigma - 6\sigma$ significance. No Fe II* $\lambda 2632$ emission is detected (Figure 1). The fluxes in the non-resonant transitions Fe II* $\lambda 2365$, $\lambda 2396$, $\lambda 2612$, $\lambda 2626$ transitions are $1.2 - 2.4 - 1.5 - 2.7 \times 10^{-18}$ ergs s $^{-1}$ cm $^{-2}$, respectively. Table 3 gives the emission peak fluxes and rest-frame equivalent widths measured for all of the Fe II* transitions. These flux ratios of 0.5 : 1.0 : 0.6 : 1.0 are consistent with the expectation (0.66 : 1.0 : 0.66 : 1.0) for optically thick gas discussed in Tang et al. (2014). In the optically thin regime, the flux ratios should be on the order of ~ 1 .

Regarding the non-detection of Fe II* $\lambda 2632$, we note that this transition is usually not detected in stacked spectra (Talia et al. 2012; Kornei et al. 2013; Tang et al. 2014; Zhu et al. 2015), except for in the Erb et al. (2012) stacked spectrum, but that it is observed in the other individual cases (Rubin et al. 2011; Martin et al. 2013). Tang et al. (2014) explore whether underlying stellar absorption suppresses the Fe II* $\lambda 2632$ emission in their stacked spectra. However, for this starburst galaxy, the F- and G-type stars that produce the underlying absorption are unlikely to significantly contribute to the stellar continuum.

We perform a joint Gaussian fit to the four non-resonant Fe II* emission peaks and find that they appear symmetric and centered on the galaxy systemic redshift measured from [O II] $\lambda\lambda 3727, 3729$ (Figure 3). This is in contrast to Zhu et al. (2015), who found that the Fe II* emission from their stacked spectrum of 8,600 galaxies is slightly asymmetric, and in contrast to Rubin et al. (2011), who observed Fe II* emission peaks that are slightly (~ 30 km s $^{-1}$) redshifted relative to the nebular emission lines.

5. Morphology of the Fe II* Emission

In this section, we investigate whether the Fe II* emission has a similar spatial extent and morphology as the stellar continuum and the [O II] $\lambda\lambda 3727, 3729$ emission.

For the Fe II* emission, first we produce a sub-cube of size $1.5'' \times 1.5''$ for each of the four emission lines and transform the wavelength axis to velocity space. We interpolate each sub-cube to the same velocity scale with pixels of 30 km s $^{-1}$ that span ± 930 km s $^{-1}$ and zero velocity at the galaxy systemic redshift, $z = 1.2902$.

We subtract the continuum and combine the four sub-cubes. To estimate the stellar continuum, we use the mean value from two regions redwards of the Fe II* emission peaks at $\sim \lambda 2425$ and $\sim \lambda 2700$ Å that span 115 Å and 300 Å respectively. The continuum pseudo narrow band image shown in Figure 4 (middle left) is from the mean of these two continuum regions, which have a flat slope.

From the combined Fe II* emission velocity cube, we then extract a narrow band (NB) image by summing 13 pixels (± 390 km s $^{-1}$). The top left panel of Figure 4 shows the pseudo-narrow band Fe II* image with 2×2 smoothing, and we use this image for the analysis. For comparison, we also tested an automated extraction with the CubExtractor software (Cantalupo et al. in prep.), which selects connected volume pixels (voxels) that are above a specified SNR threshold (2.7 was optimal in our case) to produce optimally extracted images, as in Borisova et al. (2016). Our morphological results are independent of the method used to produce the Fe II* NB image.

Similarly, we create the [O II] pseudo-narrow band image from a 30×30 pixel ($1.5'' \times 1.5''$) sub-cube that spans 18 spectral pixels (22.5 Å) to cover the $\lambda\lambda 3727, 3729$ doublet. Again, we subtract the continuum estimated between $\sim 3550 - 3600$ Å

to obtain the [O II] surface brightness map shown in the bottom left panel of Figure 4.

The Fe II* map in Figure 4 is the first two-dimensional spatial map of the Fe II* non-resonant emission in an individual galaxy at intermediate redshift. Previous studies have looked for signatures of extended Fe II* emission in stacked spectra (Erb et al. 2012; Tang et al. 2014). In a stacked spectrum from 95 star-forming galaxies at $1 < z < 2$, Erb et al. (2012) found that the Fe II* $\lambda 2626$ emission line is slightly more spatially extended than the stellar continuum. Tang et al. (2014) performed a similar analysis with 97 star-forming galaxies at $1 \lesssim z \lesssim 2.6$, but were not able to spatially resolve the Fe II* emission.

Thanks to the sensitivity of MUSE, we are able to address whether Fe II* is more extended than the continuum and to characterize the Fe II* emission morphology for the first time. The top left panel of Figure 4 shows that the extended Fe II* emission (solid contour) appears to be more extended than the continuum (dashed contour) and has a privileged direction. Comparing the Fe II* emission position angle with the kinematic axis of the galaxy, indicated with crosses, shows that the Fe II* is more extended along the minor kinematic axis of the galaxy.

To quantify the extent of the Fe II*, stellar continuum, and [O II] $\lambda\lambda 3727, 3729$ emission, we use a custom Python MCMC algorithm to fit each of the surface brightness maps in the left column of Figure 4 with a Sersic profile. The fit provides us with intrinsic parameters and with an intrinsic model of the emitting region, i.e. *deconvolved from the seeing*, because we convolve the Sersic profile with the actual PSF taken from the brightest star in the same data cube, MUSE HDFS ID#1 (see Bacon et al. 2015), across wavelengths corresponding to the galaxy emission lines⁵. In practice, we fix the Sersic index n to $n = 1$ or $n = 0.5$ because the Sersic index n is unconstrained⁶. The size estimate, $R_{1/2}$, is nonetheless robust and independent of the Sersic index n , since it is determined empirically from the flux growth curve, an integrated quantity.

Table 4 summarizes the results from this analysis and Figure 4 (middle column) shows the modeled profiles for $n = 1$ for the Fe II*, stellar continuum, and [O II] emission. The right column of Figure 4 gives the residual maps, which are the difference between the observed data and the intrinsic model convolved with the seeing.

The stellar continuum emission (Figure 4, middle row) appears round and compact. The intrinsic emission from the exponential disk fit yields an inclination of $28 \pm 3^\circ$ and a half-light radius, $R_{1/2}$, of around $0.28 \pm 0.02''$ (2.34 ± 0.17 kpc). These continuum emission properties from MUSE are comparable to the measurements from HST images discussed in Section 3 and shown in Table 1. The [O II] $\lambda\lambda 3727, 3729$ emitting region has the same morphology but is slightly more extended than the stellar continuum with $R_{1/2, [\text{O II}]} = 0.33 \pm 0.02''$ (2.76 ± 0.17 kpc). The corresponding star formation rate surface density is $\Sigma_{\text{SFR}} = 1.6 M_\odot \text{ kpc}^{-2}$.

The Fe II* emission has a morphology and physical extent that are different from the stellar continuum and [O II] emission. The intrinsic Fe II* emission is more elliptical with an axis ratio of $b/a = 0.57$, compared to the rounder continuum and

⁵ The PSF can be approximately described by a Moffat profile with FWHM $0.70''$ ($0.63''$) at the Fe II* and stellar continuum emission ([O II] emission) wavelengths, which corresponds to a half-light radius of $0.50''$ ($0.44''$).

⁶ The Sersic n index is unconstrained because the seeing radius is much larger than the emission. Indeed, the seeing radius is $\text{FWHM}/2 = 0.35''$, corresponding to $R_{1/2} \approx 0.5''$ for a Moffat profile, whereas the galaxy's intrinsic half-light radius $R_{1/2}$ is only $\approx 0.3''$.

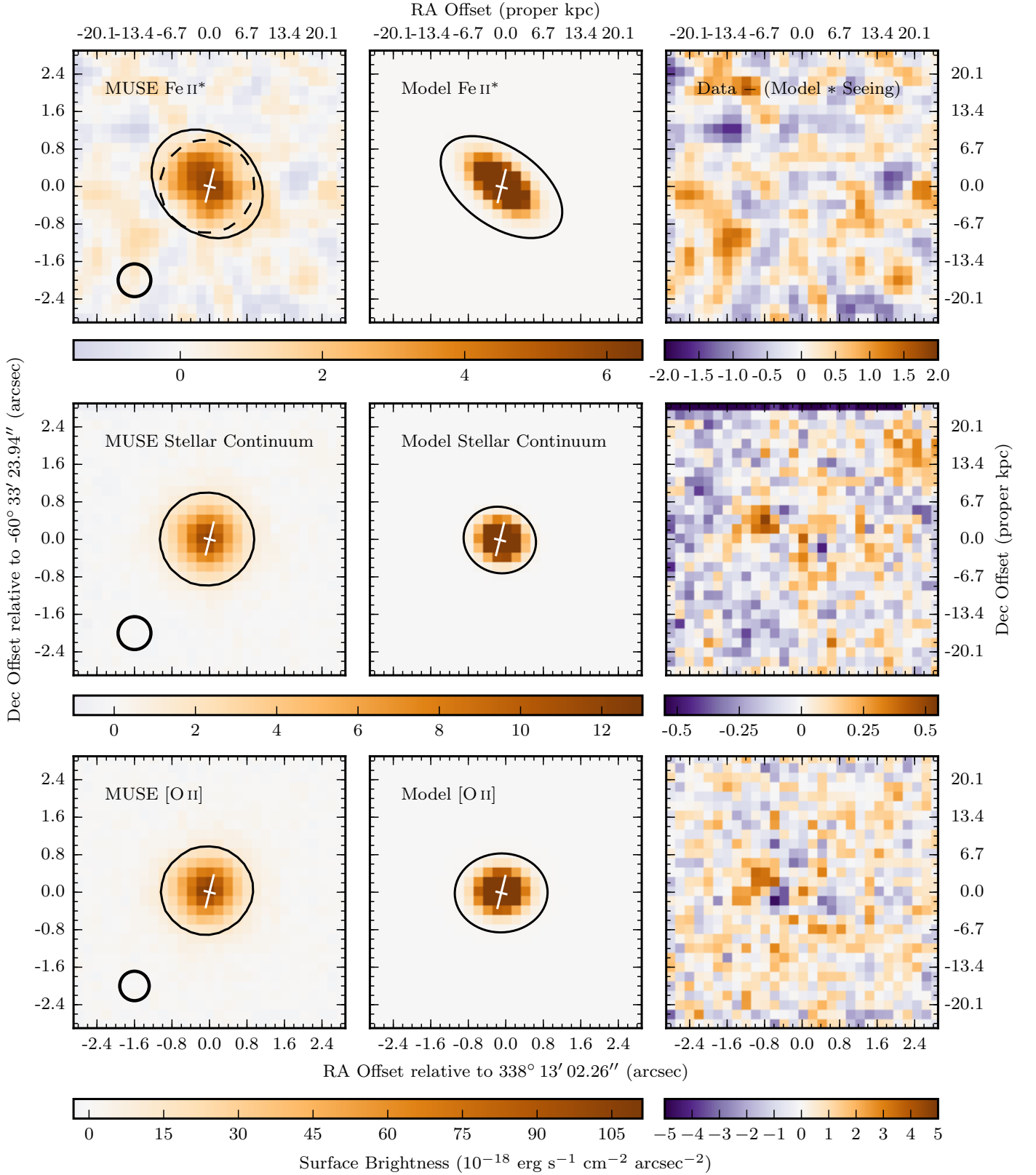


Fig. 4. *Left panels:* Surface brightness maps of Fe II* (top), stellar continuum (middle), and [O II] emission (bottom) from pseudo narrow band images (see text). Solid contours represent 1/10 of the maximum surface brightness. The dashed line in the top left panel correspond to the stellar continuum contour from middle left panel. The small black circles represent the seeing at the emission wavelength. *Middle panels:* Surface brightness maps of the intrinsic emission from an exponential disk model ‘deconvolved’ from the seeing. Ellipses in the middle column are drawn using the model parameters and have a size that corresponds to the half-light radii (see Table 4). *Right panels:* Maps of the residuals between the observed data and the intrinsic model convolved with the seeing. The white crosses indicate the galaxy major and minor axes from the Contini et al. (2016) kinematic analysis. The Fe II* emission map is more extended than both the stellar continuum or the [O II] emission.

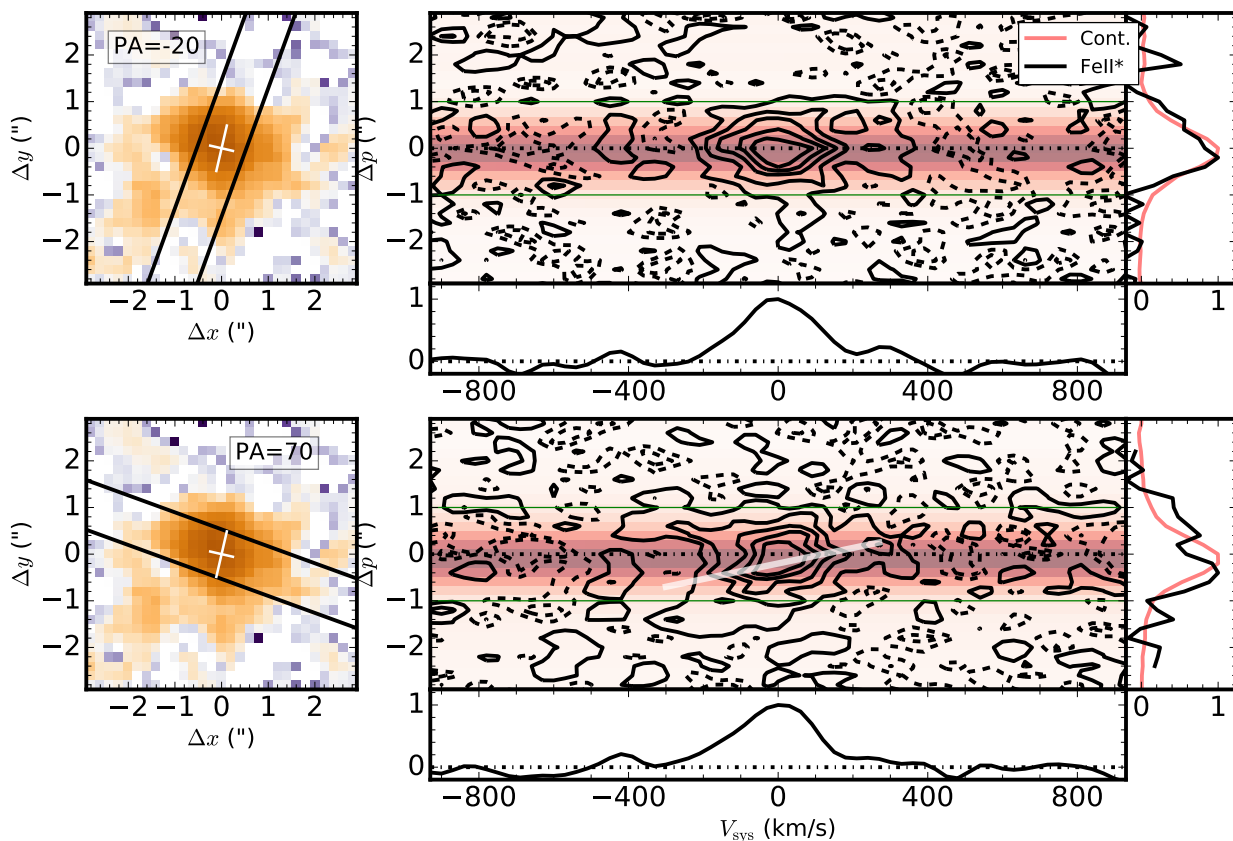


Fig. 5. *Left panels:* Narrow band images of the Fe II* emission optimally extracted from the MUSE cube shown with a 1''-wide slit oriented -20° (top) and $+70^\circ$ (bottom). The $+70^\circ$ slit orientation in the bottom panels follows the Fe II* major kinematic axis. The white crosses indicate the galaxy major and minor axes from the Contini et al. (2016) kinematic analysis of [O II]. *Right panels:* Position-velocity diagrams of the Fe II* emission from a slit oriented -20° (top) and $+70^\circ$ (bottom). Zero velocity is relative to the galaxy systemic redshift, $z = 1.29018 \pm 0.00006$, measured from the [O II] emission. Solid black contours trace Fe II* flux levels at 2, 6, 10, 14, and $18 \times 10^{-20} \text{ erg s}^{-1} \text{ cm}^{-2}$. Dashed black contours show the negative flux levels at -2 and $-4 \times 10^{-20} \text{ erg s}^{-1} \text{ cm}^{-2}$. The red gradient indicates the continuum intensity. The right side panel of each p-v diagram compares the spatial profile of the Fe II* emission (black) with that of the stellar continuum (red). The bottom sub-panel of each p-v diagram shows the total 1D flux spectrum integrated across the spatial region between the solid green horizontal lines in the p-v diagram. In the bottom p-v diagram, the white solid line follows the velocity gradients. This panel also reveals a ‘C’-shape pattern in the blue wing of the Fe II* emission extending to -400 km s^{-1} . The blue wing of the Fe II* emission is more pronounced along the slit orientation corresponding to the minor-axis (PA = $+70^\circ$).

[O II] emission, which both have $b/a \approx 0.9$. The Fe II* emission is elongated along the direction (PA $\approx +60^\circ$) that roughly corresponds to the galaxy minor kinematic axis (PA $\approx +75^\circ$, Table 1). Moreover, the intrinsic half-light radius of the Fe II* emission is $R_{1/2, \text{Fe II}^*} = 0.49 \pm 0.05''$, i.e. about 50% larger than that of the stellar continuum. In other words, the Fe II* half-light radius, $R_{1/2, \text{Fe II}^*} = 4.1 \pm 0.4 \text{ kpc}$, extends $\gtrsim 1.5 \text{ kpc}$ beyond the stellar continuum and the [O II] emission, which both have $R_{1/2} \approx 2.5 \text{ kpc}$ (Table 4). This is apparent from comparing the extent of the Fe II* emission (solid contour) to the continuum emission (dashed contour) in the top left panel of Figure 4. See Table 4 for the emission properties.

6. Kinematics of the Fe II* emission

In this section, we investigate whether it is possible to trace the kinematics of the Fe II* emission. To do so, we visually inspected the velocity cube produced in the previous section and found that the kinematic major axis from the Fe II* emission follows a PA of about 70 deg , which happens to correspond roughly to the galaxy minor kinematic axis. Figure 5 shows $p-v$ diagrams for

this 70 deg slit orientation (bottom row) and for a slit oriented at -20 deg (top row). In both cases, the slit width is $1''$. Following the peak of the Fe II* emission, we see that the Fe II* emission is elongated along the direction (PA $\approx +60^\circ$) that roughly corresponds to the galaxy minor kinematic axis. The white solid line in the bottom $p-v$ diagram guides the eye along this velocity gradient. Black contours trace the Fe II* emission, and the red shaded area indicates the continuum.

Figure 5 reveals two additional results. First, the Fe II* emission shows an extended blue-wing, which is more pronounced in the PA = $+70$ profile. Secondly, the blue-side of the Fe II* emission contours in the bottom panel, with the slit oriented at $+70 \text{ deg}$, shows a C-shaped pattern. The contours extend to -400 km s^{-1} near $+1''$ and $-1.5''$, but decrease to -200 km s^{-1} in between. This C-shape pattern is characteristic of a hollow conical emission, as could be expected from an outflow.

7. Discussion

From deep MUSE observations of the HDFs, we identify a spatially-resolved galaxy (ID#13) at $z = 1.2902$ that has a low inclination ($i = 33^\circ$), an orientation that may favor detecting

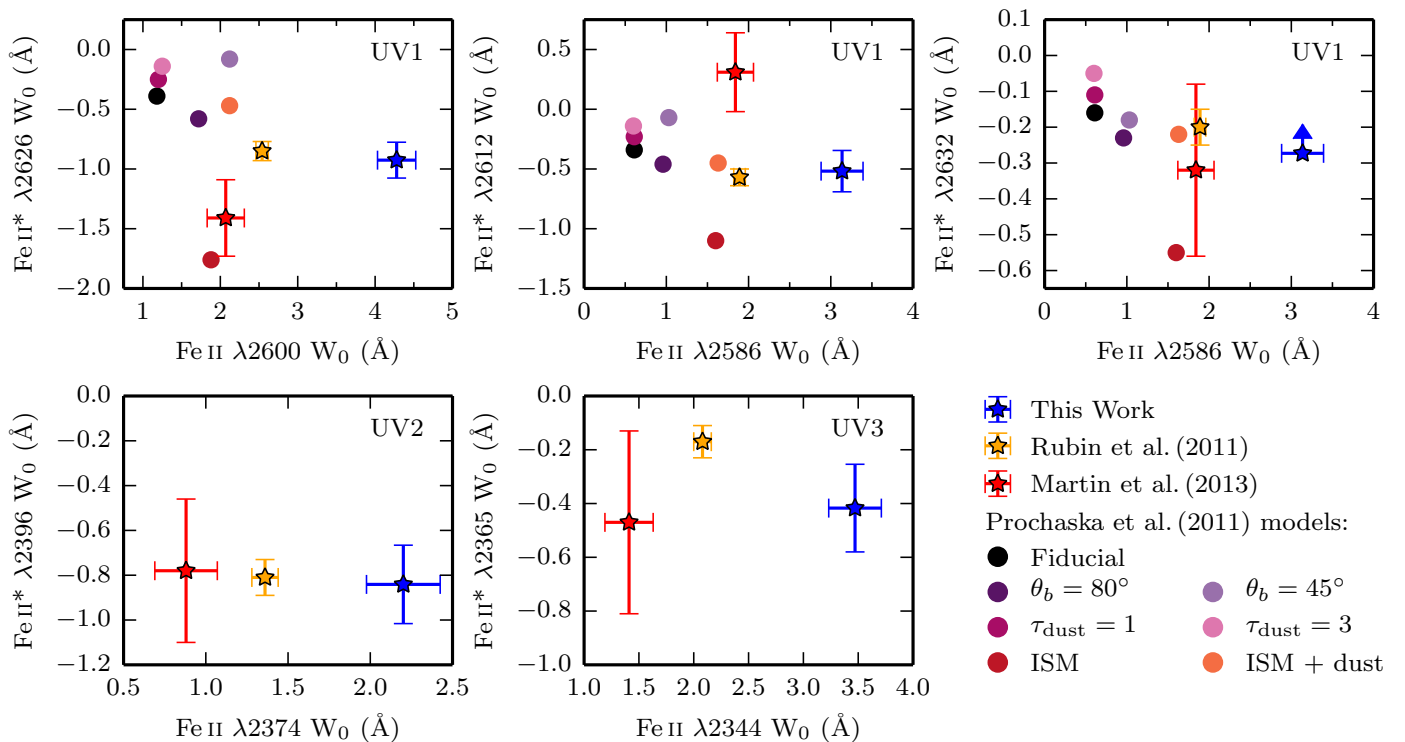


Fig. 6. Observed and modeled rest-frame equivalent widths from the Fe II UV1, UV2, and UV3 multiplet transitions. Star-shaped points indicate values measured from the three direct detections: this work (blue), Rubin et al. (2011) (yellow), and Martin et al. (2013) (red). Circular points in the top panels come from radiative transfer model predictions for the UV1 multiplet (Prochaska et al. 2011). Colors represent variations to the fiducial isotropic outflow model (black) that test different opening angles (θ_b) for bi-conical outflows, dust opacities, and include an ISM component. See Prochaska et al. (2011) for additional model variations. Model predictions for the Fe II UV2 and UV3 multiplets are not currently available.

galactic outflows in emission (Rubin et al. 2014). This galaxy has a star formation rate of $\text{SFR} = 77^{+40}_{-25} M_{\odot} \text{ yr}^{-1}$, which places it in the starburst category (See Contini et al. 2016, their Figure 3). Its star formation rate surface density is $\Sigma_{\text{SFR}} = 1.6 M_{\odot} \text{ kpc}^{-2}$, well above the threshold for galactic winds (Newman et al. 2012; Bordoloi et al. 2014). The star formation rate and stellar mass are nearly identical to those of two galaxies at $z = 0.694$ (Rubin et al. 2011) and $z = 0.9392$ (Martin et al. 2012) that both show direct evidence of galactic winds from blueshifted absorptions, redshifted Mg II emission, and non-resonant Fe II* emission.

In the integrated 1D MUSE spectrum, we detect non-resonant Fe II* emission but no apparent resonant Fe II and Mg II emission, differentiating this galaxy somewhat from the two previous examples. We also obtain the first direct detection of spatially extended Fe II* emission (Section 5) from an individual galaxy by stacking the Fe II* transitions (Figure 4). We discuss here (in Section 7.1) the implications for these results in the context of radiative transfer wind models, since the emitting gas is likely entrained in a galactic-scale outflow.

The strong, asymmetric Fe II and Mg II absorptions in the 1D galaxy spectrum, which have blueshifted components at -660 km s^{-1} and -350 km s^{-1} relative to the systemic redshift (Figure 2), are a clear signature of outflowing gas. In Section 7.2, we will estimate the mass outflow rate and compare it to the galaxy SFR.

7.1. Implications for outflow models

The MUSE surface brightness maps (Figure 4) reveal that the Fe II* emission has a more elliptical shape than the stellar continuum and the [O II] emission. Detecting Fe II* emission that is

more extended along one axis suggests that the outflow is not isotropic. Isotropic outflows are, however, the fiducial geometry for radiative transfer and semi-analytic wind models (Prochaska et al. 2011; Scarlata & Panagia 2015). Comparing these models and their variations with direct detections, such as the MUSE HDFS galaxy ID#13, can help to interpret the observations while motivating additional refinements to the models.

The radiative transfer and semi-analytic models of galactic outflows from Prochaska et al. (2011) and Scarlata & Panagia (2015) both predict concurrent resonant and non-resonant emission, because absorbed photons can be re-emitted via either non-resonant or resonant transitions for multiplets (Tang et al. 2014; Zhu et al. 2015). The spectrum of the HDFS galaxy ID#13 (Figures 1 and 2) shows strong Fe II and Mg II absorptions (with total rest-frame equivalent widths from 3 to 5 Å), but no evidence for P-cygni profiles and globally small amounts of possible emission infilling as discussed in Section 4.1. We next discuss whether this apparent lack of Fe II resonant emission occurs in other galaxies, and how to potentially reconcile the models with such data.

Like the HDFS ID#13 galaxy, the two previously published direct detections of Fe II* emission (Rubin et al. 2011; Martin et al. 2013) do not have Fe II P-cygni profiles, although they might have moderate resonant Fe II emission infilling. Unlike the HDFS ID#13 galaxy, these galaxies have strong P-cygni Mg II profiles. The published composite spectra (Talia et al. 2012; Erb et al. 2012; Kornei et al. 2013; Tang et al. 2014; Zhu et al. 2015) show non-resonant Fe II* emission without obvious resonant Fe II emission as P-cygni profiles. Among these composite spectra, only Erb et al. (2012) and Kornei et al. (2013) reveal Mg II P-cygni profiles.

In order to investigate the origin of the apparent lack of resonant Fe II emission, in Figure 6 we compare rest-frame equivalent width measurements from the MUSE HDFS ID#13 galaxy with predictions from the Prochaska et al. (2011) radiative transfer models, following Erb et al. (2012). In Figure 6, we also include the two previously published direct detections of Fe II* emission from Rubin et al. (2011) and Martin et al. (2013). Each panel pairs a non-resonant Fe II* emission transition with its corresponding resonant Fe II absorption transition from within a multiplet.

Prochaska et al. (2011) produce models for the Fe II UV1 multiplet and Mg II $\lambda\lambda 2797, 2803$ doublet to explore how varying model geometries and physical assumptions about the dust content, ISM contribution, gas density, and wind speeds impact the line profiles from the resonant and non-resonant transitions. In nearly all of the tested models, the resonant transitions produce P-cygni profiles with blueshifted absorption and redshifted emission. Varying each of the physical properties individually from the fiducial model is not sufficient to suppress the resonant Fe II and Mg II P-cygni profiles. Indeed, the only model that substantially suppresses the resonant emission combines an ISM component with dust extinction. In order to reproduce the observed profiles of the MUSE HDFS galaxy ID#13, the models will need to simultaneously incorporate more properties. To gain physical intuition for the impact of the individual properties, we now discuss varying the outflow geometry, dust extinction and ISM component affects the profiles.

In contrast to their fiducial model (black point in Figure 6), which assumes angular isotropy, Prochaska et al. (2011) also modeled bi-conical outflows (purple points), where the wind fills an opening angle into and out of the plane of the sky along the line of the sight to the galaxy. Collimating the outflow suppresses both the resonant and non-resonant emission, and for highly collimated outflows, absorption dominates the profile. The lack of resonant emission in the HDFS galaxy ID#13 suggests that the outflow could be bi-conical and collimated. However, since this geometry also suppresses the non-resonant Fe II* emission, highly collimated wind models create a double-peaked Fe II* profile that is not observed.

The Prochaska et al. (2011) fiducial model assumes no dust extinction, but they show that dust absorption (pink points in Figure 6) can have a strong impact on the line profiles. Increasing the amount of dust extinction suppresses the resonant emission slightly more than the non-resonant emission. Adding $\tau_{\text{dust}} = 3$ to the fiducial model leaves a weak Fe II P-cygni profile, whereas the model with $\tau_{\text{dust}} = 10$ suppresses the resonant Fe II emission while leaving weak non-resonant Fe II* emission. However, such copious dust extinction would extinguish the source by 15 magnitudes and make it unobservable. The moderate visual extinction for the galaxy ID#13, $A_V = 1.20^{+0.59}_{-0.26}$ mag, suggests that dust extinction alone is not sufficient to explain the diminished resonant emission.

Adapting the outflow model to include gas that represents the ISM of the galaxy (red circular point in Figure 6), i.e., gas that is centralized and lacks a significant radial velocity, also produces line profiles with similarities to the galaxy ID#13. Adding the ISM component increases the absorption around zero systemic velocity and suppresses the resonant Fe II emission. Moreover, the ISM component can boost the Fe II* emission. For Fe II, more resonant absorption due to the ISM component allows more photons to escape through non-resonant re-emission. Indeed, the non-resonant Fe II* emission becomes ~ 10 times stronger than in the fiducial model. With suppressed Fe II emission but

increased Fe II* emission, an ISM component is essential to recreating the observations from the galaxy ID#13.

Finally, Prochaska et al. (2011) include dust extinction in the ISM component (orange point in Figure 6). Compared to the dusty wind model discussed earlier, this model suffers much more from dust extinction because the simple kinematic structure of the ISM allows multiple scattering events. For Mg II, the photons are resonantly trapped in the dusty ISM. For Fe II, all of the emission lines diminish compared to the same model without dust, but the ratio between the Fe II* emission to Fe II emission remains stronger than in the fiducial model. This model best describes the ID#13 galaxy. Further exploring the same physical conditions with a bi-conical outflow may highlight subtleties that could indicate preferring one geometry over another.

To summarize, we suggest that a model combining a dusty ISM with a bi-conical outflow that has a moderate amount of dust opacity in the wind would be able to match the data for the HDFS galaxy ID#13.

7.2. Mass Outflow Rate Estimation

To estimate the mass entrained in the outflow, we consider only the absorption components that are not affected by the ISM. Consequently, we exclude the component ‘C’ at the systemic velocity (Figure 2, Table 2). The other two components are blueshifted by -660 km s^{-1} (‘A’) and -350 km s^{-1} (‘B’), respectively. The wind component ‘B’ at -350 km s^{-1} dominates the bulk of the mass flux given the equivalent width ratios between components ‘A’ and ‘B.’ As discussed in Section 4.1, the wind component ‘B’ is the least affected by emission infilling (at or below the 10% level), whereas the ISM component ‘C’ is the most affected by emission infilling. Hence, emission infilling does not affect our estimate of the mass outflow rate from the wind component ‘B.’

Similar to Rubin et al. (2014), we estimate the mass outflow rate from:

$$\frac{dM}{dt} \approx 1 M_{\odot} \text{ yr}^{-1} C_f \frac{N_{\text{flow}}(\text{H})}{10^{20} \text{ cm}^{-2}} \frac{A_{\text{flow}}}{45 \text{ kpc}^2} \frac{v}{300 \text{ km s}^{-1}} \frac{5 \text{ kpc}}{D} \quad (1)$$

where C_f is the covering fraction of the outflowing gas, $N_{\text{flow}}(\text{H})$ is the column density of hydrogen associated with the outflow, A_{flow} is the projected surface area of the outflow, v is the outflow velocity, and D is the physical distance the outflow extends from the galaxy center.

We estimate $N_{\text{flow}}(\text{H})$ from the metal column densities $N(\text{Fe})$ and $N(\text{Mg})$. Because VPFIT column densities and Doppler b parameters are degenerate for optically thick lines, we determine the metal column densities $N(\text{Fe})$ and $N(\text{Mg})$ from the equivalent width, W_0 , following Spitzer (1968), with an additional term for the covering fraction:

$$\log N = \log \frac{W_0}{\lambda} - \log \frac{2F(\tau_0)}{\pi^{1/2} \tau_0} - \log \lambda f - \log C_f + 20.053 \quad (2)$$

where τ_0 is the optical depth at line center, λ is the transition wavelength in \AA , and f is the oscillator strength. The optical depth τ_0 is determined from the ratio of equivalent widths from two lines within the same multiplet, as in Weiner et al. (2009); Rubin et al. (2010b), which is referred to as the ‘doublet ratio’ method.

For Mg II, the oscillator strengths indicate that the equivalent width ratio is 2 : 1 in the optically thin case. The Mg II equivalent width ratio follows $F(2\tau_0)/F(\tau_0)$ for the transmission integral:

$$F(\tau_0) = \int_0^{+\infty} (1 - e^{-\tau_0 \exp(-x^2)}) dx \quad (3)$$

From our measured Mg II equivalent width ratio, 1.06 ± 0.13 , we numerically solve for $\tau_{0,2803} \approx 240$. Both the equivalent width ratio and the high optical depth value indicate that Mg II is saturated.

For Fe II, we can calculate the optical depth for two different sets of transitions: $\tau_{0,2586}$ from $W_{0,2600}/W_{0,2586}$ and $\tau_{0,2374}$ from $W_{0,2382}/W_{0,2374}$. The optical depth ratios are $3.46 : 1$ and $10.22 : 1$ respectively, using the oscillator strength values from Morton (2003). After again solving numerically, the optical depth values are $\tau_{0,2586} = 3.53$ and $\tau_{0,2374} = 1.55$. We can therefore use these optical depth and equivalent width values to obtain a good estimate of the Fe II column density, since Jenkins (1986) find accurate column densities even for blended components that result from multiple clouds, as long as the optical depth in the weaker transition is $\tau_0 < 5$.

With knowledge of the optical depth, we can determine the covering fraction from the residual intensities between the zero level and the doublet lines (Rupke et al. 2005; Sato et al. 2009; Martin & Bouché 2009; Martin et al. 2012; Rubin et al. 2014). Using Equation 5 from Rupke et al. (2005) with Mg II, we find a covering fraction of at least 0.4. However, this formula ignores the instrument resolution, which could lead to a much higher covering fraction. To estimate a lower limit on the column density, we take $C_f = 1$, as in Rubin et al. (2010b).

Applying Equation 2, the column density measurements are $N(\text{Mg II } \lambda 2803) = 15.89$, $N(\text{Fe II } \lambda 2586) = 14.74$, and $N(\text{Fe II } \lambda 2374) = 14.76$. These measurements are in good agreement with the values from vpFit, $N(\text{Mg II}) = 15.87 \pm 0.68$ and $N(\text{Fe II}) = 14.75 \pm 0.16$.

From the metal column densities, in order to estimate the gas flow column density $N_{\text{flow}}(\text{H})$, we use solar abundances (with $\log(\text{Mg}/\text{H}) = -4.40$ and $\log(\text{Fe}/\text{H}) = -4.50$; Asplund et al. 2009) and a dust depletion correction but no ionization correction, as in Rubin et al. (2011). To estimate the dust depletion factor, we use the Jenkins (2009) method to simultaneously fit for the depletion level using the column densities of these two elements (Mg, Fe). The fit yields a global depletion factor of $F_\star = 1.25 \pm 0.39$, corresponding to δFe of -2.60 dex and δMg of -1.50 dex. With these depletion corrections, the total gas column density is thus at least $\log N(\text{H}) \geq 21.76 \pm 0.48 - \log Z/Z_\odot$, given that we used solar abundances⁷.

We can estimate the projected area of the outflow A_{flow} from the size of the stellar continuum, since we detect Mg II and Fe II in absorption against the continuum. The MUSE stellar continuum (Section 5) has an intrinsic half-light radius of 2.34 ± 0.17 kpc. Because the spectrum is optimally extracted with a white-light image weighting scheme, the *effective* half-light radius of the extracted 1D spectrum is $R_{1/2,\text{eff}} = \sqrt{2} \times R_{1/2,\star}$ or 3.3 kpc. The stellar continuum therefore covers a surface area of $A_{\text{flow}} = \pi R_{1/2,\star}^2 b/a = 30 \text{ kpc}^2$.

Finally, we must assume an effective or characteristic distance for the gas at -350 km/s with a total column of $\log N_{\text{flow}}(\text{H}) > 21.80$. For a mass-conserving flow, the gas closer to the galaxy will dominate the column density. However, outflowing gas moving at -350 km s⁻¹ needs a few kpc (1–5) to accelerate to that speed (Murray et al. 2011). Hence, we conservatively use an upper limit of $D < 5$ kpc, as in Rubin et al. (2014), which leads to an outflow rate of $> 45 \text{ M}_\odot \text{ yr}^{-1}$. For plausible values of 2–3 kpc, the outflow rate would be $75 - 110 \text{ M}_\odot \text{ yr}^{-1}$. In comparison, the Fe II* emission has a characteristic size of

~ 4 kpc. Overall, the outflow rate is comparable to the star formation rate of $78 \text{ M}_\odot \text{ yr}^{-1}$.

8. Conclusions

The direct detection of Fe II* emission from the spatially-resolved MUSE HDFS galaxy ID#13 at $z = 1.29$ opens a new avenue for studying galactic outflows in emission. From an analysis of the deepest MUSE field so far (27 hours), the properties of this individual galaxy, including the inclination, stellar mass, star formation rate, and gas kinematics, are well characterized (Table 1). This galaxy has a low inclination ($i \sim 33$ deg), $M_\star = 8 \times 10^9 \text{ M}_\odot$, and $\text{SFR} = 77_{-25}^{+40} \text{ M}_\odot \text{ yr}^{-1}$.

Using the 1D integrated spectrum and 2D pseudo-narrow band images, we identify signatures of winds in emission from the Fe II*, Fe II, and Mg II transitions and investigate the wind morphology and extent. Specifically, we find:

- The star formation rate surface density from [O II] $\lambda\lambda 3727, 3729$ is $\Sigma_{\text{SFR}} = 1.6 \text{ M}_\odot \text{ kpc}^{-2}$, well above the threshold for galactic winds (Newman et al. 2012; Bordoloi et al. 2014).
- Asymmetric Fe II, Mg II, and Mg I self-absorptions in the MUSE 1D spectrum have a strong blue wing that extends beyond $\sim -700 \text{ km s}^{-1}$. The profiles are well-fitted with three components at -660 km s^{-1} , -350 km s^{-1} , and $+9 \text{ km s}^{-1}$ (Figure 2). These blue-shifted absorptions indicate outflowing material along the line of sight, and we estimate a mass outflow rate in the range of $45 - 110 \text{ M}_\odot \text{ yr}^{-1}$.
- Emission infilling does not appear to be present because (i) all absorptions have very similar shapes, whereas infilling varies significantly for different transitions (Zhu et al. 2015) and (ii) the strongest component for all absorptions (including Fe II $\lambda 2600$ and $\lambda 2382$) is close to the galaxy systemic redshift (Figure 2). A quantitative analysis following the Zhu et al. (2015) empirical method shows that emission infilling could impact the Fe II $\lambda 2600$ (Fe II $\lambda 2383$) rest-frame equivalent width by at most 10% (25%), respectively, and less for the other Fe II transitions.
- Non-resonant Fe II* emission from the $\lambda 2365$, $\lambda 2396$, $\lambda 2612$, and $\lambda 2626$ transitions have fluxes of $1.2 - 2.4 - 1.5 - 2.7 \times 10^{18} \text{ egs s}^{-1} \text{ cm}^{-2}$, respectively, and flux ratios that are consistent with optically thick gas (Tang et al. 2014). The Fe II* $\lambda 2632$ transition has a $1-\sigma$ flux limit of $< 8 \times 10^{-19} \text{ egs s}^{-1} \text{ cm}^{-2}$. Contrary to stacked spectra (e.g. Zhu et al. 2015), the Fe II* emission in this galaxy appear to be symmetric and well-centered on the galaxy [O II] systemic redshift (Figure 3).
- After stacking the four non-resonant Fe II* emission lines, we obtain the first spatially-resolved 2D map of this non-resonant emission from a $z \sim 1$ galaxy (Figure 4). The Fe II* emission is more extended than the stellar continuum or [O II] emission. The Fe II* emission half-light radius is $R_{1/2,\text{Fe II}^*} = 4.1 \pm 0.4 \text{ kpc}$, about 50% larger than that of the continuum which has $R_{1/2,\star} = 2.34 \pm 0.17 \text{ kpc}$. The Fe II* emission has a different morphology; it is more elongated in the direction that roughly corresponds to the galaxy minor kinematic axis.
- The Fe II* emission displays a velocity gradient along the kinematic minor axis, and the blue wing of the emission contours reveals a C-shape pattern in a $p - v$ diagram from a pseudo-slit extracted along this axis (Figure 5). These features are consistent with a conical outflow.

⁷ Ionization corrections would further increase the column density, but they are small at this level.

- Comparing the observed emission and absorption properties with predictions (Figure 6) from the radiative transfer models of Prochaska et al. (2011) suggests that the isotropic fiducial wind model fails, but that a biconical wind model including a dusty ISM component could more likely reproduce the observations from galaxy ID#13.

This geometry agrees with a growing body of models and observations that suggest outflowing gas driven by supernovae explosions escapes the disk preferentially along the galaxy minor axis in a bi-conical flow (e.g., Chen et al. 2010; Bordoloi et al. 2011; Bouché et al. 2012; Kornei et al. 2013; Kacprzak et al. 2012; Martin et al. 2012).

Fe II* emission from the MUSE HDFS galaxy ID#13 was identified serendipitously, but by systematically searching through field galaxies in similar IFU data sets it will be possible to construct samples of $z \sim 1$ galaxies that each show evidence of outflows in emission. Observational constraints from these samples can then drive improvements to models of galactic-scale outflows.

Acknowledgements. This work has been carried out thanks to the support of the ANR FOGHAR (ANR-13-BS05-0010-02), the OCEVU Labex (ANR-11-LABX-0060), and the A*MIDEX project (ANR-11-IDEX-0001-02) funded by the “Investissements d’avenir” French government program. NB acknowledges support from a Career Integration Grant (CIG) (PCIG11-GA-2012-321702) within the 7th European Community Framework Program. RB acknowledges support from the ERC advanced grant 339659-MUSICOS. JB is supported by FCT through Investigador FCT contract IF/01654/2014/CP1215/CT0003, by Fundação para a Ciência e a Tecnologia (FCT) through national funds (UID/FIS/04434/2013), and by FEDER through COMPETE2020 (POCI-01-0145-FEDER-007672). BE acknowledges support from the “Programme National de Cosmologie and Galaxies” (PNCG) of CNRS/INSU, France. RAM acknowledges support by the Swiss National Science Foundation. JR acknowledges support from the ERC starting grant 336736-CALENDS.

References

Adelberger, K. L., Shapley, A. E., Steidel, C. C., et al. 2005, *ApJ*, 629, 636
 Arribas, S., Colina, L., Bellocchi, E., Maiolino, R., & Villar-Martín, M. 2014, *A&A*, 568, A14
 Asplund, M., Grevesse, N., Sauval, A. J., & Scott, P. 2009, *ARA&A*, 47, 481
 Bacon, R., Brinchmann, J., Richard, J., et al. 2015, *A&A*, 575, A75
 Berry, M., Gawiser, E., Guaita, L., et al. 2012, *ApJ*, 749, 4
 Bordoloi, R., Lilly, S. J., Kacprzak, G. G., & Churchill, C. W. 2014, *ApJ*, 784, 108
 Bordoloi, R., Lilly, S. J., Knobel, C., et al. 2011, *ApJ*, 743, 10
 Bordoloi, R., Rigby, J. R., Tumlinson, J., et al. 2016, *MNRAS*, 458, 1891
 Borisova, E., Cantalupo, S., Lilly, S. J., et al. 2016, *ApJ*, 831, 39
 Bouché, N., Carfantan, H., Schroetter, I., Michel-Dansac, L., & Contini, T. 2015, *AJ*, 150, 92
 Bouché, N., Finley, H., Schroetter, I., et al. 2016, *ApJ*, 820, 121
 Bouché, N., Hohensee, W., Vargas, R., et al. 2012, *MNRAS*, 426, 801
 Cazzoli, G., Lattanzi, V., Kirsch, T., et al. 2016, *A&A*, 591, A126
 Cecil, G., Bland-Hawthorn, J., Veilleux, S., & Filippenko, A. V. 2001, *ApJ*, 555, 338
 Chabrier, G. 2003, *ApJ*, 586, L133
 Chen, Y.-M., Tremonti, C. A., Heckman, T. M., et al. 2010, *AJ*, 140, 445
 Chisholm, J., Tremonti, C. A., Leitherer, C., et al. 2015, *ApJ*, 811, 149
 Cicone, C., Maiolino, R., & Marconi, A. 2016, *A&A*, 588, A41
 Coil, A. L., Weiner, B. J., Holz, D. E., et al. 2011, *ApJ*, 743, 46
 Contini, T., Epinat, B., Bouché, N., et al. 2016, *A&A*, 591, A49
 Diamond-Stanic, A. M., Coil, A. L., Moustakas, J., et al. 2016, *ApJ*, 824, 24
 Dutta, R., Srianand, R., Gupta, N., et al. 2017, *MNRAS*, 465, 4249
 Elbaz, D., Daddi, E., Le Borgne, D., et al. 2007, *A&A*, 468, 33
 Epinat, B., Tasca, L., Amram, P., et al. 2012, *A&A*, 539, A92
 Erb, D. K., Quider, A. M., Henry, A. L., & Martin, C. L. 2012, *ApJ*, 759, 26
 Finlator, K. & Davé, R. 2008, *MNRAS*, 385, 2181
 Ford, A. B., Werk, J. K., Davé, R., et al. 2016, *MNRAS*, 459, 1745
 García-Burillo, S., Combes, F., Usero, A., et al. 2015, *A&A*, 580, A35
 Genzel, R., Newman, S., Jones, T., et al. 2011, *ApJ*, 733, 101
 Heckman, T. M., Alexandroff, R. M., Borthakur, S., Overzier, R., & Leitherer, C. 2015, *ApJ*, 809, 147
 Heckman, T. M., Dahlem, M., Lehnert, M. D., et al. 1995, *ApJ*, 448, 98

Jaskot, A. E. & Oey, M. S. 2014, *ApJ*, 791, L19
 Jenkins, E. B. 1986, *ApJ*, 304, 739
 Jenkins, E. B. 2009, *ApJ*, 700, 1299
 Kacprzak, G. G., Churchill, C. W., & Nielsen, N. M. 2012, *ApJ*, 760, L7
 Karim, A., Schinnerer, E., Martínez-Sansigre, A., et al. 2011, *ApJ*, 730, 61
 Karman, W., Grillo, C., Balestra, I., et al. 2016, *A&A*, 585, A27
 Kewley, L. J., Geller, M. J., & Jansen, R. A. 2004, *AJ*, 127, 2002
 Kornei, K. A., Shapley, A. E., Martin, C. L., et al. 2012, *ApJ*, 758, 135
 Kornei, K. A., Shapley, A. E., Martin, C. L., et al. 2013, *ApJ*, 774, 50
 Lehnert, M. D., Heckman, T. M., & Weaver, K. A. 1999, *ApJ*, 523, 575
 Lilly, S. J., Carollo, C. M., Pipino, A., Renzini, A., & Peng, Y. 2013, *ApJ*, 772, 119
 Martin, C. L. & Bouché, N. 2009, *ApJ*, 703, 1394
 Martin, C. L., Shapley, A. E., Coil, A. L., et al. 2012, *ApJ*, 760, 127
 Martin, C. L., Shapley, A. E., Coil, A. L., et al. 2013, *ApJ*, 770, 41
 Matsubayashi, K., Sugai, H., Hattori, T., et al. 2009, *ApJ*, 701, 1636
 Matsuda, Y., Yamada, T., Hayashino, T., et al. 2012, *MNRAS*, 425, 878
 Moiseev, A., Karachentsev, I., & Kaisin, S. 2010, *MNRAS*, 403, 1849
 Morrissey, P., Matuszewski, M., Martin, C., et al. 2012, in *Proc. SPIE*, Vol. 8446, Ground-based and Airborne Instrumentation for Astronomy IV, 844613
 Morton, D. C. 2003, *ApJS*, 149, 205
 Murray, N., Ménard, B., & Thompson, T. A. 2011, *ApJ*, 735, 66
 Newman, S. F., Genzel, R., Förster-Schreiber, N. M., et al. 2012, *ApJ*, 761, 43
 Oppenheimer, B. D. & Davé, R. 2008, *MNRAS*, 387, 577
 Peng, C. Y., Ho, L. C., Impey, C. D., & Rix, H.-W. 2002, *AJ*, 124, 266
 Péroux, C., Quiret, S., Rahmani, H., et al. 2016, *MNRAS*, 457, 903
 Prochaska, J. X., Kasen, D., & Rubin, K. 2011, *ApJ*, 734, 24
 Rigby, J. R., Bayliss, M. B., Gladders, M. D., et al. 2014, *ApJ*, 790, 44
 Rubin, K. H. R., Prochaska, J. X., Koo, D. C., et al. 2014, *ApJ*, 794, 156
 Rubin, K. H. R., Prochaska, J. X., Koo, D. C., Phillips, A. C., & Weiner, B. J. 2010a, *ApJ*, 712, 574
 Rubin, K. H. R., Prochaska, J. X., Ménard, B., et al. 2011, *ApJ*, 728, 55
 Rubin, K. H. R., Weiner, B. J., Koo, D. C., et al. 2010b, *ApJ*, 719, 1503
 Rupke, D. S., Veilleux, S., & Sanders, D. B. 2005, *ApJS*, 160, 87
 Sato, T., Martin, C. L., Noeske, K. G., Koo, D. C., & Lotz, J. M. 2009, *ApJ*, 696, 214
 Scarlata, C. & Panagia, N. 2015, *ApJ*, 801, 43
 Schroetter, I., Bouché, N., Péroux, C., et al. 2015, *ApJ*, 804, 83
 Schroetter, I., Bouché, N., Wendt, M., et al. 2016, *ArXiv e-prints* [arXiv:1605.03412]
 Shapley, A. E., Steidel, C. C., Pettini, M., & Adelberger, K. L. 2003, *ApJ*, 588, 65
 Shopbell, P. L. & Bland-Hawthorn, J. 1998, *ApJ*, 493, 129
 Silk, J. & Mamon, G. A. 2012, *Research in Astronomy and Astrophysics*, 12, 917
 Soto, K. T. & Martin, C. L. 2012, *ApJS*, 203, 3
 Spitzer, L. 1968, *Diffuse matter in space*
 Steidel, C. C., Bogosavljević, M., Shapley, A. E., et al. 2011, *ApJ*, 736, 160
 Steidel, C. C., Erb, D. K., Shapley, A. E., et al. 2010, *ApJ*, 717, 289
 Straka, L. A., Johnson, S., York, D. G., et al. 2016, *MNRAS*, 458, 3760
 Talia, M., Mignoli, M., Cimatti, A., et al. 2012, *A&A*, 539, A61
 Tang, Y., Gialvalisco, M., Guo, Y., & Kurk, J. 2014, *ApJ*, 793, 92
 Tomczak, A. R., Quadri, R. F., Tran, K.-V. H., et al. 2016, *ApJ*, 817, 118
 Tremonti, C. A., Heckman, T. M., Kauffmann, G., et al. 2004, *ApJ*, 613, 898
 Veilleux, S., Cecil, G., & Bland-Hawthorn, J. 2005, *ARA&A*, 43, 769
 Veilleux, S. & Rupke, D. S. 2002, *ApJ*, 565, L63
 Weiner, B. J., Coil, A. L., Prochaska, J. X., et al. 2009, *ApJ*, 692, 187
 Whitaker, K. E., Franx, M., Leja, J., et al. 2014, *ApJ*, 795, 104
 Wisotzki, L., Bacon, R., Blaizot, J., et al. 2016, *A&A*, 587, A98
 Wood, C. M., Tremonti, C. A., Calzetti, D., et al. 2015, *MNRAS*, 452, 2712
 Zhu, G. B., Comparat, J., Kneib, J.-P., et al. 2015, *ApJ*, 815, 48

Table 2. Absorption rest-frame equivalent widths for the three sub-components in Figure 2

Components		A	B	C	Total	
Redshift		1.28514	1.28752	1.29024		
Δv (km s ⁻¹)		-660 ± 28	-349 ± 12	+8.5 ± 6.5		
Transition	Multiplet	$W_{0,\text{fit}}$ (Å)	$W_{0,\text{fit}}$ (Å)	$W_{0,\text{fit}}$ (Å)	$W_{0,\text{fit}}$ (Å)	$W_{0,\text{flux}}$ (Å)
(1)	(2)	(3)	(4)	(5)	(6)	(7)
Fe II λ 2344	FeII UV3	0.13	0.93	2.06	3.09	3.47±0.24
Fe II λ 2374	FeII UV2	0.04	0.55	1.70	2.42	2.20±0.22
Fe II λ 2382	FeII UV2 ^a	0.24	1.17	2.36	3.69	3.27±0.22
Fe II λ 2586	FeII UV1	0.10	0.91	2.15	3.14	3.14±0.26
Fe II λ 2600	FeII UV1	0.24	1.24	2.52	3.97	4.28±0.25
Mg II λ 2796		0.98	1.64	2.82	5.51	5.09±0.18
Mg II λ 2803		0.93	1.89	2.63	4.47	4.90±0.17
Mg I λ 2853		0.16	0.49	0.31	0.94	0.86±0.21

Notes. Column (1): Absorption line. Column (2): Multiplet associated with transition. Column (3): Equivalent width for component A. Column (4): Equivalent width for component B. Column (5): Equivalent width for component C. Column (6): Total equivalent width measured from fits. Column (7): Total equivalent width measured from the spectrum.

^(a) Fe II λ 2382 is a pure resonant absorption line with no associated Fe II* emission.

Table 3. Emission and absorption rest-frame equivalent width and flux values

Multiplet	λ Å	E_{high} cm ⁻¹	E_{low} cm ⁻¹	J	A_{ul} s ⁻¹	W_0 Å	Flux 10 ⁻¹⁸ egs s ⁻¹ cm ⁻²
(1)	(2)	(3)	(4)	(5)	(6)	(7)	(8)
Fe II UV1	2600.17	38458.98	0.00	9/2←9/2	Absorption	4.28 ± 0.25	...
	2626.45	38458.98	384.79	9/2→7/2	3.41E+07	-0.93 ± 0.13	2.67 ± 0.43
	2586.65	38660.04	0.00	7/2←9/2	Absorption	3.14 ± 0.26	...
	2612.65	38660.04	384.79	7/2→7/2	1.23E+08	-0.53 ± 0.15	1.47 ± 0.49
	2632.11	38660.04	667.68	7/2→5/2	6.21E+07	> -0.27	< 0.78 ± 0.42
Fe II UV2	2382.76	41968.05	0.00	11/2←9/2	Absorption ^a	3.27 ± 0.22	...
	2374.46	42114.82	0.00	9/2←9/2	Absorption	2.20 ± 0.22	...
	2396.36	42114.82	384.79	9/2→7/2	2.67E+08	-0.84 ± 0.17	2.37 ± 0.49
Fe II UV3	2344.21	42658.22	0.00	7/2←9/2	Absorption	3.47 ± 0.24	...
	2365.55	42658.22	384.79	7/2→7/2	5.90E+07	-0.42 ± 0.15	1.22 ± 0.48
	2381.49	42658.22	667.68	7/2→5/2	3.10E+07 ^b
C II]	2324.21	43025.3	0.00	3/2→1/2	...		
	2325.40	43003.3	0.00	1/2→1/2	...		
	2326.11	43053.6	63.42	5/2→3/2	...	-1.03 ± 0.18	2.83 ± 0.50
	2327.64	43025.3	63.42	3/2→3/2	...		
	2328.83	43003.3	63.42	1/2→3/2	...		
[O II]	3727.10	26830.57	0.00	3/2 →3/2	...	-48.98 ± 0.29	133.46 ± 0.80
	3729.86	26810.55	0.00	5/2 →3/2	...		

Notes. Column (1): Transition name. Column (2): Transition wavelength. Column (3): Upper energy level. Column (4): Lower energy level. Column (5): Level total angular momentum quantum number J . Column (6): Einstein A_{ul} coefficient for spontaneous emission. Column (7): Rest-frame equivalent width. Column (8): Line flux.

^(a) Fe II λ 2382 is a pure resonant transition with no associated Fe II* emission. ^(b) Fe II* λ 2381 emission is blended with Fe II λ 2382 absorption.

Table 4. Summary of two-dimensional morphological analysis

	Fe II*	Stellar Continuum	[O II]
Axis ratio	0.57 ± 0.01	0.90 ± 0.02	0.85 ± 0.01
$R_{1/2}$ (arcsec)	0.49 ± 0.05	0.28 ± 0.02	0.33 ± 0.02
$R_{1/2}$ (kpc)	4.1 ± 0.4	2.34 ± 0.17	2.76 ± 0.17